The Journal of Chemical Physics

Femtosecond bond breaking and charge dynamics in ultracharged amino acids

Cite as: J. Chem. Phys. **151**, 144307 (2019); https://doi.org/10.1063/1.5116814
Submitted: 08 July 2019 . Accepted: 17 September 2019 . Published Online: 11 October 2019

Oscar Grånäs, Nicusor Timneanu, Ibrahim Eliah Dawod, Davide Ragazzon, Sebastian Trygg, Petros Souvatzis, Tomas Edvinsson, and Carl Caleman

COLLECTIONS

Paper published as part of the special topic on Ultrafast molecular sciences by femtosecond photons and electrons

Note: The paper is part of the JCP Special Topic on Ultrafast Molecular Sciences by Femtosecond Photons and Electrons.

View Online Export Citation CrossMark

ARTICLES YOU MAY BE INTERESTED IN

Hybrid plasmonic metasurfaces
Journal of Applied Physics **126**, 140901 (2019); https://doi.org/10.1063/1.5116885

Elucidation of the photoaquation reaction mechanism in ferrous hexacyanide using synchrotron x-rays with sub-pulse-duration sensitivity
The Journal of Chemical Physics **151**, 144306 (2019); https://doi.org/10.1063/1.5117318

Alignment of morphology during high spatial frequency periodic structure formation in GaAs
Journal of Applied Physics **126**, 143102 (2019); https://doi.org/10.1063/1.5114930

Lock-in Amplifiers
Zurich Instruments
Watch the Video ▶

© 2019 Author(s).

AIP Publishing

The Journal of Chemical Physics ARTICLE scitation.org/journal/jcp

Femtosecond bond breaking and charge dynamics in ultracharged amino acids

Cite as: J. Chem. Phys. **151**, 144307 (2019); doi: 10.1063/1.5116814
Submitted: 8 July 2019 • Accepted: 17 September 2019 •
Published Online: 11 October 2019

Oscar Grånäs,[1,a] **Nicusor Timneanu,**[1] **Ibrahim Eliah Dawod,**[1] **Davide Ragazzon,**[1] **Sebastian Trygg,**[1] **Petros Souvatzis,**[1] **Tomas Edvinsson,**[2] **and Carl Caleman**[1,3,b]

AFFILIATIONS

[1] Department of Physics and Astronomy, Uppsala University, Box 516, SE-751 20 Uppsala, Sweden
[2] Department of Engineering Sciences, Uppsala University, Box 534, SE-751 21 Uppsala, Sweden
[3] Center for Free-Electron Laser Science, Deutsches Elektronen-Synchrotron, Notkestraße 85, DE-22607 Hamburg, Germany

Note: The paper is part of the JCP Special Topic on Ultrafast Molecular Sciences by Femtosecond Photons and Electrons.

[a] oscar.granas@physics.uu.se
[b] carl.caleman@physics.uu.se

ABSTRACT

Historically, structure determination of nanocrystals, proteins, and macromolecules required the growth of high-quality crystals sufficiently large to diffract X-rays efficiently while withstanding radiation damage. The development of the X-ray free-electron laser has opened the path toward high resolution single particle imaging, and the extreme intensity of the X-rays ensures that enough diffraction statistics are collected before the sample is destroyed by radiation damage. Still, recovery of the structure is a challenge, in part due to the partial fragmentation of the sample during the diffraction event. In this study, we use first-principles based methods to study the impact of radiation induced ionization of six amino acids on the reconstruction process. In particular, we study the fragmentation and charge rearrangement to elucidate the time scales involved and the characteristic fragments occurring.

© 2019 Author(s). All article content, except where otherwise noted, is licensed under a Creative Commons Attribution (CC BY) license (http://creativecommons.org/licenses/by/4.0/). https://doi.org/10.1063/1.5116814

I. INTRODUCTION

In 2000, it was predicted that imaging of proteins using X-ray free-electron laser (XFEL) pulses could be done without the need of crystals.[1] Since then, a number of XFEL sources have been commissioned and are now accessible to the research community. The Linac Coherent Light Source (LCLS) in Stanford was the first XFEL reaching a photon energy high enough to achieve atomic resolution. Recently, the European XFEL was also opened for users. Even if the scientific output from LCLS has been impressive, the main contributions within structural biology have been done using crystalline samples. However, major efforts have been put into developing the imaging of single noncrystalline biomolecules (SPI),[2] and in this specific scientific case, it has been one of the main drives pushing the significant investments into developing high repetition rate XFEL sources such as LCLS II and the European XFEL.

Exposing any sample to the intense X-ray exposure from an XFEL source will cause major ionization and ultimately destroy the sample that is investigated. Radiation damage in these types of experiments has been a concern since the idea was first presented. For a crystalline sample, it has been shown that it is possible to achieve atomic resolution, despite the fact that the sample is destroyed during the exposure. This is explained by the fact that the scattered signal is gated by the loss of order in the sample, as described by Barty *et al.*[3] For SPI, the situation is more complex since the X-rays are not scattered into Bragg peaks. However, a recent publication indicates that radiation damage of single proteins exposed to an XFEL pulse might not be as problematic as was initially thought.[4] During the time a sample is exposed to the XFEL pulse, the diffracted signal decreases due to the loss of bound electrons and the loss of spatial coherence in the sample (due to the atomic displacement). Hence, the unperturbed sample scatters more than the ionized sample, resulting in a diffracted signal with a bias toward the nondamaged sample. Even if we consider these mechanisms, radiation damage will ultimately add to the noise in the diffracted signal, which, in

© Author(s) 2019

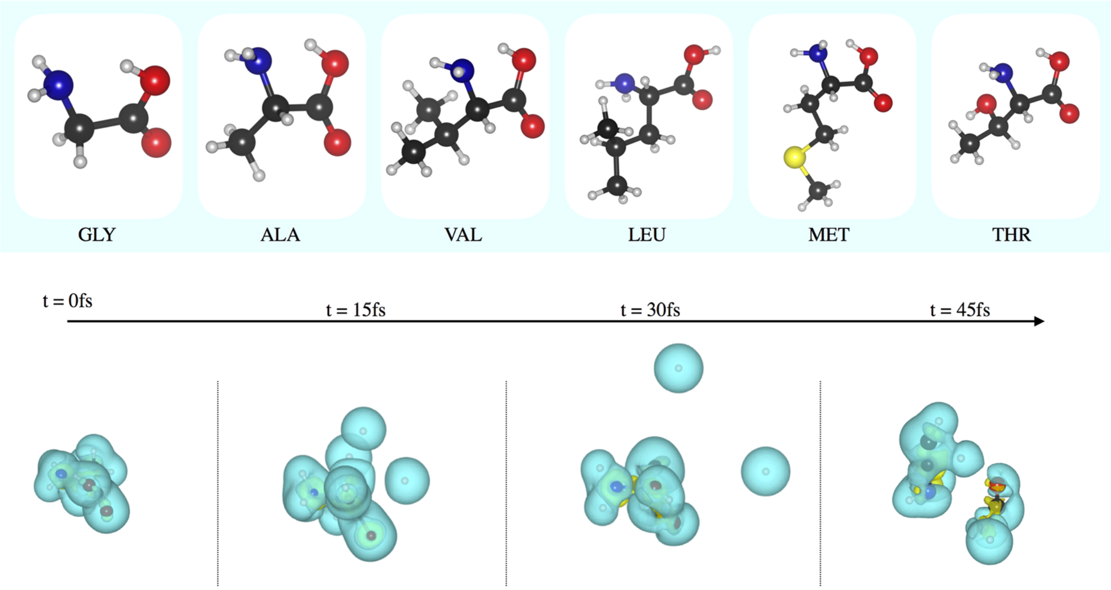

FIG. 1. (Top) Graphical representation of the six amino acids studied and (bottom) Snapshots from a single trajectory of an alanine (ALA) at $\bar{z} = 1$, showing both the positions of the nuclei and the isosurface of the electron density. Isosurface contributions colored in blue are associated with electron density depletion, whereas yellow indicates the electron density increase. The typical trajectory shows a typical behavior with some hydrogen atoms detaching first, followed by a fragmentation where the bond to the carboxyl group is severed.

turn, results in a lower resolution of the final molecular structure.

Studying femtosecond bond breaking and charge dynamics in ultracharged biomolecules is not relevant only for imaging using XFEL pulses. The idea of using electron diffraction for imaging has been around for decades.[5,6] Recent efforts to develop sources capable of delivering electron pulses which are intense and short enough for electron diffraction imaging have vitalized the topic.[7–9] Imaging biomolecules using electron pulses is limited by radiation damage in the same way as imaging using XFEL pulses.[10]

Fragmentation of organic molecules has been studied for decades, motivated by a range of different scientific questions. The ionization of DNA using kilo-electron-volt ions is biologically relevant for ion and proton tumor therapy, and it has been shown that the structure of nucleobases[11–15] as well as deoxyribose[16] is very sensitive to the keV ion impact. In the field of mass spectrometry, the fragmentation of amino acids due to protonation has been studied extensively.[17,18] In the perspective of the present study, the most relevant experimental studies are probably high resolution coincidence time-of-flight mass spectrometry or similar techniques, which have, for example, been used to study the fragmentation of alanine caused by kilo-electron-volt ions such as He^+, He^{2+}, and O^{5+}.[19]

Using amino acids as a prototype system, we are able to follow both changes in the electronic distribution and the movement of the ions in a combined quantum mechanical and molecular mechanical approach.[20,47] We would like to stress that, for example, the peptide bond and solvent pH alter the attachments of hydrogens and perturbs the electronic structure of the amino acids. However, the consistency of hydrogen dissociation, regardless of what atoms it is bonded to, leads us to expect that this has only minor influence under the ultracharged conditions which we perform our simulations in. Our choice of prototype system and computational methods aim to strike a balance between the relevant size of the molecule, rigorous statistical sampling of initial conditions, and the theoretical description of the coupled electronic and ionic trajectories following ionization.

The use of molecular mechanics based on force-fields allows for thermalization of the amino acid structure in a water environment, and the quantum mechanical modeling allows us to follow the dynamics of both the nuclei and the electron distribution of highly ionized amino acids. In this way, we are able to identify damage processes specific to protein molecules, which in turn will be of valuable knowledge in the reconstruction process. The full method of the simulations is presented in Sec. II. In short, we have studied six amino acids: glycine (GLY), alanine (ALA), valine (VAL), leucine (LEU), methionine (MET), and threonine (THR) (see Fig. 1). Each amino acid is ionized stepwise up to an average ionization of +1 per atom, here denoted as $\bar{z} = 1$. The simulations are 75 fs long, and the ionizations are introduced at the beginning of the simulation.

II. METHODS

In this section, we describe the computational workflow as well as the methods used. In order to capture as much of the relevant processes as possible, we use a set of simulation methods with different capabilities. For the ultrafast processes addressed in this work, the assumptions that certain degrees of freedom can be considered fixed while studying the details of others cannot be made. For example, ionization happens on time scales shorter than the time scale

© Author(s) 2019

of the vibrational modes of the bonds, possibly leading to an initial state dependence. By sampling many trajectories, we are able to average out the dependence on the initial state in order to produce a general result. The trajectories, denoted as T_i in Fig. 2, are initiated from nonionized thermalized starting geometries, as described in Subsection II A. From each starting trajectory, we spawn quantum molecular dynamics trajectories for a number of ionization levels covering the range +1 to $+N$, where N is the total number of atoms in the molecule. For each ionization level, each amino acid is sampled by 10 trajectories, resulting in an average of 168 trajectories per amino acid. The standard error of the bond integrity is sufficiently low in comparison to the standard deviation to give satisfactory statistics to draw a general conclusion. The level of ionization per atom is denoted as $\bar{z}$, where $0 < \bar{z} \leq 1$. The main technique used for simulating the ionization and bond breaking is described in Subsection II B. In order to validate how the computational description of the ionized molecule affects the bond breaking, we test, in addition to our main technique, two complementary methods as described in Subsection II C.

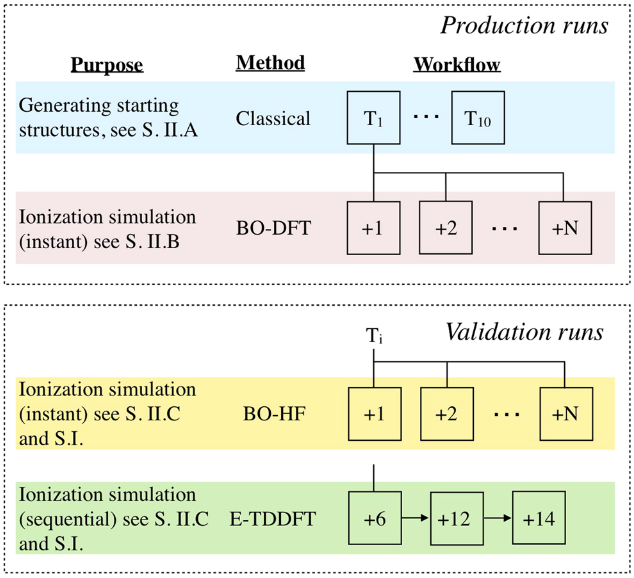
Production runs
Purpose
Method
Workflow
Generating starting structures, see S. II.A
Classical
T1
T10
Ionization simulation (instant) see S. II.B
BO-DFT
+1
+2
+N
Validation runs
Ti
Ionization simulation (instant) see S. II.C and S.I.
BO-HF
+1
+2
+N
Ionization simulation (sequential) see S. II.C and S.I.
E-TDDFT
+6
+12
+14

FIG. 2. Flow chart of the work-process including the purpose and method of simulation, including a reference to the corresponding section where detailed information can be found. Starting configurations are generated using classical molecular dynamics, where an aqueous environment is included, and ten different thermalized trajectories for each amino acid are generated, denoted as T_i. Subsequently, quantum molecular dynamics based on density functional theory within the Born-Oppenheimer density functional theory (BO-DFT) approximation is used to study the trajectories of the ionized molecules. In the production runs, the level of ionization is initiated from the first time step and all integer levels up to a charge of $+N$ are simulated. In order to validate the influence of our treatment of the ionization processes, we assess the bond breaking procedure according to two additional methods: Hartree-Fock (HF) within the Born-Oppenheimer (BO-HF) and nonadiabatic time-dependent density functional theory (TDDFT) as formulated in the real-time domain with Ehrenfest molecular dynamics (E-TDDFT). We also compare the influence of ionizing the molecule from the first time step to a sequential procedure. Details of these tests are supplied in the supplementary material.

A. Generating starting structures

To sample appropriate starting configurations, we ran 10 independent molecular dynamics simulations of our six molecules. These presimulations were done using the *GROMACS* software package,[23–26] and the molecules were solvated in a $2 \times 2 \times 2$ nm box of water. A water environment, in contrast to vacuum, was picked to mimic the situation in a protein crystal or inside a living organism. Simulations were done at 300 K, using the Berendsen temperature coupling,[27] with a coupling constant of 0.1 ps. The simulations were done with a time step of 2 fs. We employed a 1.1 nm cutoff for Lennard-Jones interactions and the same distance as the switching distance for the particle mesh Ewald algorithm for computing Coulomb interactions.[28,29] The simulations from which the final starting structures were taken were 100 ps long, and we ensured that the total energy drift was less than 1% during the simulation. Following earlier work,[30,31] the structures were optimized using the Gaussian 03 suite of programs[32] at the HF level with the $6\text{-}311\text{G}^{**}$ basis.[33–37] We used the Generalized Amber Force Field (GAFF)[38] together with the TIP3P[39] water model for the simulations. The choice of the force field is probably not crucial for generating decent starting structures, and the use of the GAFF is based on its generality and our prior experience. Simulations of small organic molecules in water using several different force fields indicate that our choice of the force field is suited for these types of simulations.[40]

B. Ionization simulations

In an electron diffraction experiment, electron impact ionization primarily affects the valence electrons. Hence, core electrons can be expected not to contribute to the bond breaking and charge redistribution. From a point of view of an XFEL imaging experiment, the core electrons might initially seem like the main ingredient since the most probable primary ionization event in an XFEL experiment at a photon energy of 8 keV is by a photon removing an inner shell electron. However, following the primary photoionization, secondary electron impact ionization will occur in the sample. From one single photoionization event, several hundred secondary ionizations may occur,[42,43] depending on the photon intensity. These electron impact ionizations occur mainly through the removal of a valence shell electron, i.e., a low energy electron, similar to the electron diffraction experiment. Hence, the core-hole is, in the end, not expected to dominate the stability. In addition to the fact that the ratio of primary photoionization to secondary impact ionization is small, the core-hole life-time in these systems is expected to be short in relation to the time scales of the ionic motion due to the efficiency of recombination through Auger emission or X-ray fluorescence.

Following the above-mentioned physical considerations and the fact that a significant number of trajectories need to be sampled to avoid artifacts from different initial conditions, our production runs are in the framework of pseudo-potential density functional theory (DFT) in conjunction with Born-Oppenheimer molecular dynamics as implemented in the *Siesta*-package.[20] We assume that the electronic ground-state at a specific ionization level, as provided by DFT in the Born-Oppenheimer approximation, is more strongly bound than the excited electronic configurations. Hence, we expect to have an upper estimate of stability times *in vacuo*. The wave-functions are expanded in terms of numerical atom-centered

© Author(s) 2019

basis functions, where we use a so called triple-zeta + double polarization orbitals basis set, allowing sufficient variational freedom to relax the density for each ionization step. The vicinity of the core is described by norm-conserving pseudo-potentials of the Kleinman-Bylander type.[44] We generate extra hard pseudo-potentials (cutoff radii of 0.97 Å and 0.85 Å for *s* and *p* electrons and 0.87 Å for both *d* and *f*). The hardness of the pseudo-potentials requires a grid cutoff of 500 Ry for accurate integration. The exchange-correlation functional adopted is the generalized gradient approximation (GGA) by Perdew, Burke, and Ernzerhof (PBE).[45] Ionization is performed in steps, always assuming the sudden approximation. This means that at a geometric snapshot, the molecule is ionized to some degree, with a charge density that is assumed to be thermalized, occupied according to the aufbau principle to the electron number required to reach a certain level of ionization. It is known from plasma simulations that the electronic temperature rapidly increases with the ionization level.[46] To account for this, the electronic temperature T_e was linearly increased with the level of ionization, from 0 K at the charge neutral molecule up to $N \cdot 1000$ K at the maximally ionized molecule. The run-time for each of the N ionization steps for each of the 10 geometries is 75 fs to ensure enough time to dissociate the molecule.

C. Validation simulations

The main approximations of the technique used for the ionization simulations involve the Born-Oppenheimer approximation (in the implementations used to assume that electrons are in the ground-state of the respective ionization level) and the exchange-correlation treatment within density functional theory. To estimate the impact of these approximations, we perform a limited number of calculations with more computationally demanding methods for the validation purpose. Here, we focus on the bond breaking in the glycine molecule using 1) Hartree-Fock (HF) as implemented in the UQUANTCHEM code[41] and 2) implementation of time-dependent density functional theory in the real-time domain with Ehrenfest molecular dynamics.[21] HF is generally considered inferior to DFT when calculating molecular stability due to the complete lack of correlation.[48] However, the inclusion of only exact-exchange is an important scenario, where the knowledge that Hartree-Fock overestimates atomization energies allows us to some degree to bracket the most physical scenario of these highly ionized molecules.

TD-DFT in conjunction with Ehrenfest molecular dynamics relaxes the Born-Oppenheimer approximation; hence, we are able to describe electrons in excited states as well. The state-preparation technique for the excited states that we employ here is a fully self-consistent ΔSCF scheme.[21] In our TD-DFT benchmark, we simulate, in addition to the ground-state, only the lowest excitation due to the computational expense.

We also test how sensitive the time scale of bond breaking is to how the ionization is performed. In the supplementary material, we display bond breaking characteristics of the glycine molecule in Figs. SI.11 and SI.12 when we perform ionization sequentially in contrast to the instant ionization performed for our production simulations. It is clear that due to the ultrafast ionization process, the outcome is not sensitive to this treatment. Consult the supplementary material for further information.

Using the two methodologies, we are able to capture the effects of the exact exchange and the impact of a low-lying excited state on the dissociation pattern. The validation procedure shows that we should expect a qualitative result from our primary method, in line with what is expected from comparisons of DFT with respect to high level quantum chemistry methods.[22] In addition, the density redistribution is expected to be well reproduced. In the supplementary material, we compare the bond integrity of the glycine C–C* and C–O bonds, resulting from a DFT calculations with that of unrestricted Hartree-Fock calculations, as depicted in Fig. SI.10. Similarly, we compare the ground-state to exited state bond integrity for a single trajectory of glycine based on real-time TD-DFT with Ehrenfest molecular dynamics, as seen in Figs. SI.11 and SI.12. The general trends are the same using the three methods, which makes us convinced that what we observe are not the effects caused by the method we have chosen. Some difference can be identified though. However, for low ionization levels, the Hartree-Fock results for the C–O bond differ from those of DFT and TD-DFT. We attribute this to the overbinding nature of Hartree-Fock and the lack of screening. This makes the bond stable to slightly higher ionization in HF than in DFT.

D. Analysis

The susceptibility to the breaking of a chemical bond between two atoms, A, and B, was estimated by the so-called chemical bond integrity, $\mathscr{B}_I(A,B)$, defined by

$$\mathscr{B}_I(A,B,t) = \frac{1}{N_{MD}} \sum_{i=1}^{N_{MD}} \left(1 + e^{\lambda(|d_i[A,B](t) - d_i[A,B](0)| - 0.5)}\right)^{-1}. \qquad (1)$$

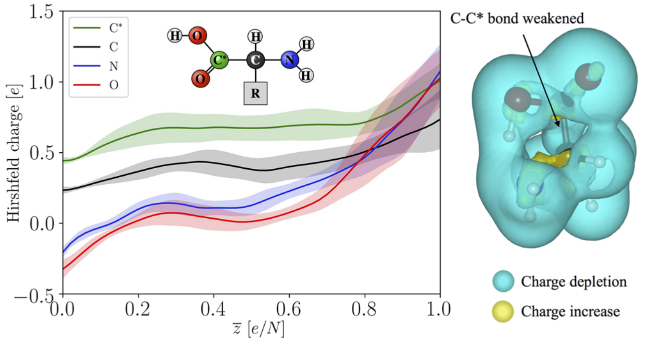

FIG. 3. On the left hand side, the deviation from the neutral charge state per ionization stage, averaged over all trajectories and amino acids. The shaded area corresponds to the area encapsulating one standard deviation. The statistical analysis is performed over all ten trajectories for all ionization stages for all amino acids, resulting in 1010 data-points for each atom type. We used a cubic interpolation to access the same $\bar{z}$, which is needed because the different number of atoms in the molecules results in different ratios of charge to atoms. Atoms crucial for the structural integrity of peptides and proteins are included. On the right hand side, we rationalize the weakness of the C–C* bond by investigating the difference in charge density between the ionized state and the ground state for a representative amino acid (alanine with an ionization degree of 5, equaling roughly $\bar{z} = 0.4$). We can see that in some parts of the molecule, the charge density is, in fact, *increased* due to the reduced electronic screening caused by the ionization. This is not the case for the C–C* bond, which is consistently weakened.

© Author(s) 2019

Here, $d_i[A, B](t)$ is the distance between atoms A and B at the simulation time t for the i-th MD-simulation, $N_{MD}(=10)$ is the number of MD-simulations performed, and λ (here = 10) is an arbitrary smearing parameter chosen in such a way that normal bond oscillations are not captured as a broken bond. For values $\mathscr{B} \approx 1$, the atoms are at their initial positions for the particular end point of the MD simulation used to generate the starting structure, corresponding to a stable bond. When $\mathscr{B} \approx 0$, the deviation from the initial distance between the atoms is large, indicating a broken bond. In the figures of bond breaking, values close to 1 are yellow and values close to zero are purple.

The Hirshfeld charge is based on the division of the system into well defined atomic fragments.[49] The charge density is, at each point, shared between the atoms proportionally to the free atom densities at the corresponding distance from the nuclei. The atomic charges are defined by an integration of the bonded minus the nonbonded atoms.[21,49] The density difference between bonded and free atom is the so-called deformation density, which can be integrated to give a distinct measure for how charge redistribution should be associated with a specific ion. The Hirshfeld partitioning scheme has proven to be one of the most robust charge partitioning schemes with respect to numerical details of the calculations.[50] The Hirshfeld charges are reported to be somewhat smaller in magnitude with respect to other methods but has an advantage that the net charges necessarily converges when the molecular deformation density converges to the true solution.[51] For the present study, this is a good measurement of the charge distribution since we are interested in the relative changes.

III. RESULTS

The aim of this study is to identify trends in the bond breaking that could help us understand how the amino acids are fragmented in an imaging experiment. We focus on finding generalized bonding and scattering properties that are similar between different amino acids. In the perspective of macromolecular imaging experiments,

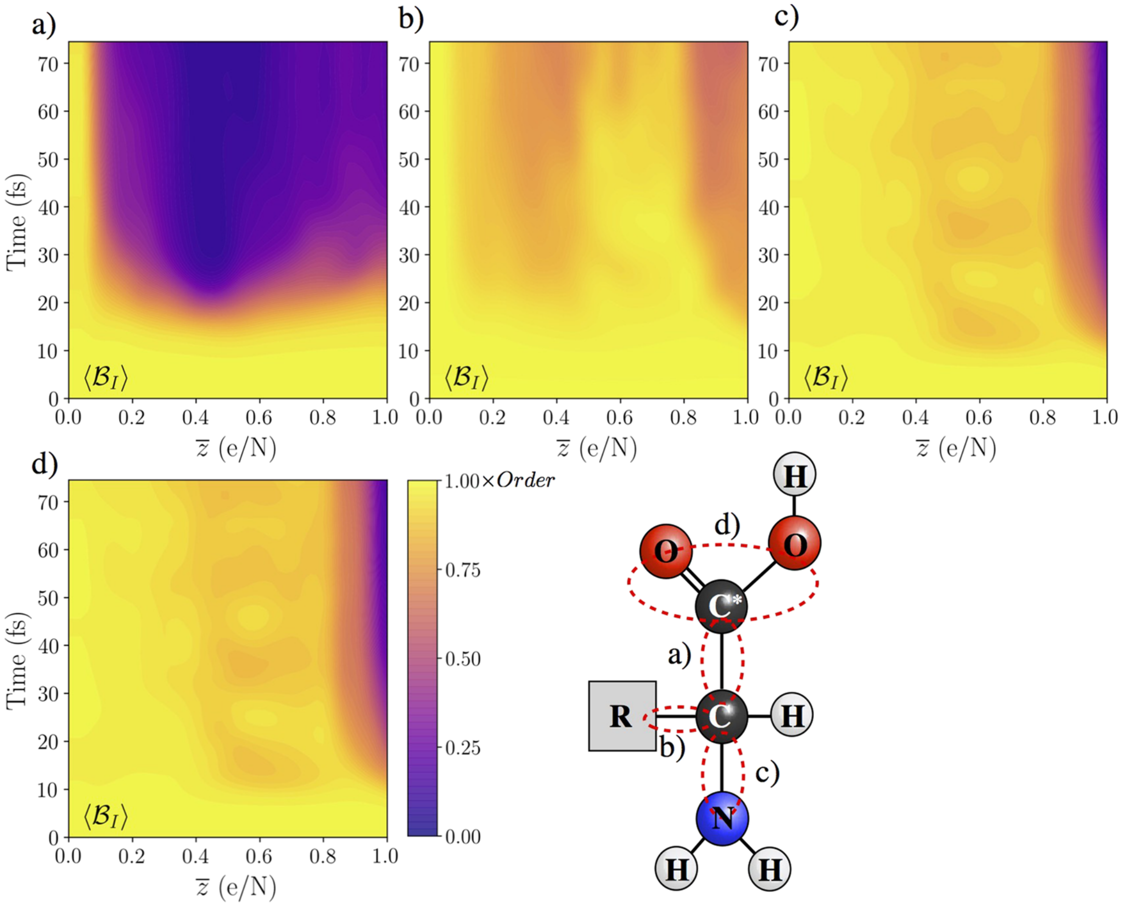

FIG. 4. Mean bond integrity as described by equation (IID) for the (a) C–C* bond, (b) C–R bond, (c) C–N bond, and (d) C–O bonds in the backbone. Statistics for all trajectories for all six amino acids are accounted for. The color gradient indicates the probability of the bond being broken, the scale goes from 0 (purple) to 1 (yellow) with the number of equivalent bonds taken into account, i.e., the carboxyl oxygen has two equivalent bonds, and a bond integrity of 0.5 means, on average, one of the bonds are broken. It is evident from our calculations that the C–C* bond is rather sensitive to ionization. The C–N and C–O bonds break at an ionization level of approximately $\overline{z} = 1$, whereas the C–R bond seems to be most robust with respect to ionization.

© Author(s) 2019

the dynamics of specific amino acids is less relevant than general trends that hold for more than a specific amino acid species. We simulate multiple trajectories for the six amino acids, followed by a comprehensive statistical approach; we deduce information of the probable dissociation pathways of the amino acids as a function of time and ionization level. The main cause of dissociation is ionization followed by charge redistribution. In addition, the redistribution of electrons potentially alters the scattering cross sections of individual ions on the molecular fragments. Snapshots from a single trajectory of an alanine with an average ionization per atom of $\bar{z} = 0.5$ can be seen in Fig. 1, showing both the positions of the nuclei and the isosurface of the electron density.

We first analyze how the electron density distribution changes in the ionized ground states of the respective amino acid. Subsequently, we analyze general trends in the breaking of molecular bonds, and finally, we investigate trends for individual differences in particular bond breaking conditions. The main individual differences come from (i) the number of hydrogen atoms and (ii) the number of bonds in the amino acid. In the supplementary material, bond breaking results for all individual amino acids are available.

A. Charge redistribution

The charge redistribution is crucial for describing the ionization process and the effective scattering cross section of each ion. In this section, we review how the charge is redistributed as a function of time and ionization degree. In order to associate the redistribution of electron density with a specific ion, we use the charge-density partitioning scheme by Hirshfeld *et al.*, as described in Subsection II D. Redistribution of charge, indicating a different relative electron count between different atoms than is expected in the free atom ground state, is important to track possible changes in scattering intensity. The elastic X-ray scattering power of an atom or ion is related to the number of bound electrons. In cases where the Hirshfeld charge of two different ion species changes in a way that they become impossible to tell apart, it can, in principle, affect the ability to determine the atomic species using X-ray diffraction. In Fig. 3, we show the deviation from the neutral atom of the Hirshfeld charge for four important atom types in the amino acids. The data shown are the average of all amino acids simulated, integrated over the full trajectories of the simulation for each degree of ionization. Focusing on the internal order of the four graphs, we see that at ionizations up

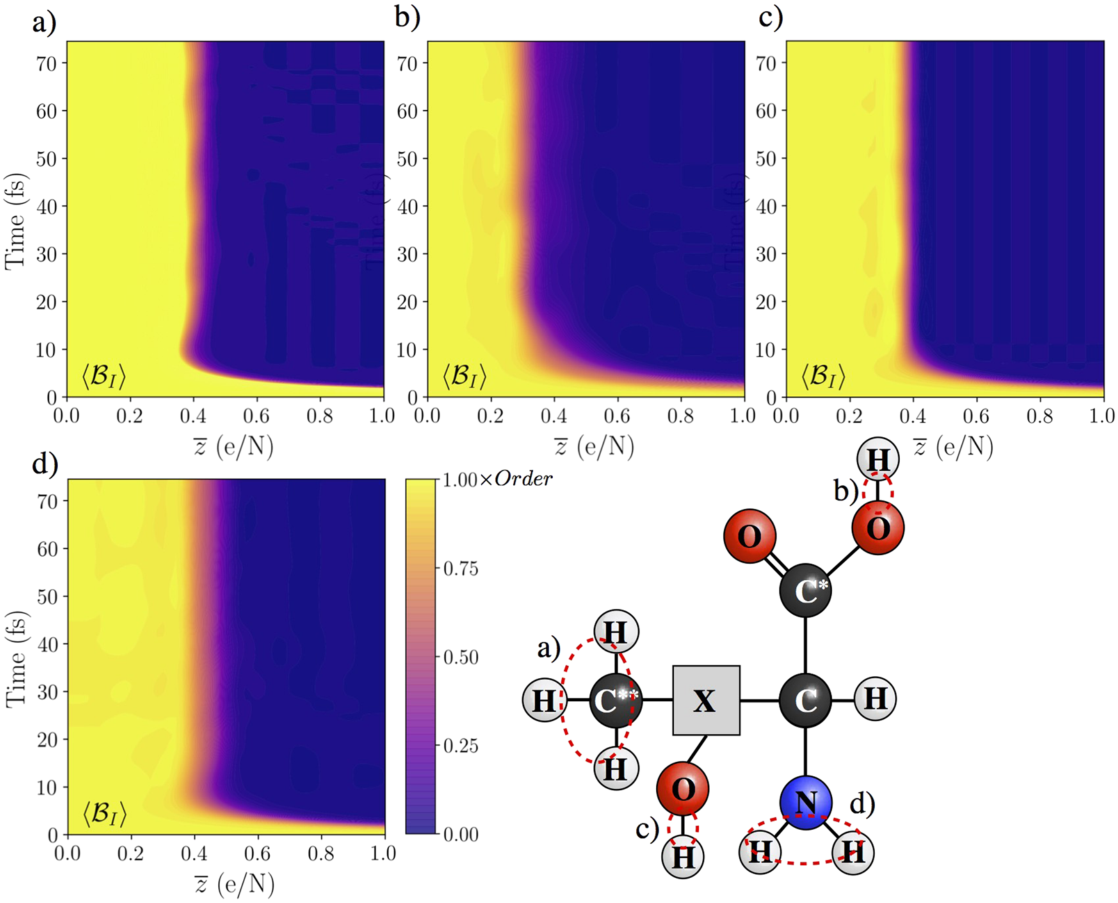

FIG. 5. Bond integrity of the bonds to hydrogen on the (a) methyl, (b) carboxyl, (c) hydroxyl, and (d) amine groups. All hydrogen atoms show a similar stability with respect to ionization.

© Author(s) 2019

to $\bar{z} = 0.7$, the order stays the same. However, above $\bar{z} = 0.8$, the oxygen and the nitrogen get a higher charge than the two other atom types. They also have very similar charges. The charge follows the nature of the bond breaking. As displayed in Fig. 3, we can see that in some parts of the molecule, the charge density is, in fact, *increased* due to the reduced electronic screening due to ionization. This provides stability to certain bonds to high levels of ionization. However, this is not the case for the C–C* bond, which is consistently weakened.

Again looking at the oxygen and the nitrogen atoms, their charges increase until the point where the hydrogens leave after 5–10 fs at around $\bar{z} = 0.35$—compare Figs. 5 and 3. As a consequence, the charge on oxygen and nitrogen actually decreases again. The next observation is that at around $\bar{z} = 0.7$, the carbon-oxygen bonds as well as the carbon-nitrogen bonds are broken, and at ionization states higher than this, bonds to the next carbon are broken (Fig. 4). To understand this, it is important to remember that in this study the ionization level is set at the first time step—before any bond is broken. In the highest ionization state, most bonds are broken early in the simulation and the atoms behave more like isolated ions, which explains why three of the four atom types shown in the figure end up at a charge of +1. They are simply monoatomic ions with the charge +1 during most of the simulations. For the backbone C, black line in the figure, this is not the case. Instead, the bond to the side chain stays unbroken for most of the simulations even at $\bar{z} = 1$, allowing for partial Hirshfeld charges.

B. Bond breaking in the backbone

Next, we study the bonds that in a peptide or protein structure are associated with the backbone structure, i.e., the bond between the α-carbon to the carbon in the carboxyl group (denoted as C–C*) and the α-carbon to the nitrogen in the amino group (denoted as C–N). To compare the bond breaking, we have defined a bond integrity parameter (described in Sec. II), indicating if a bond is broken or not. Comparing Figs. 4(a) and 4(c), it is clear that the C–N bond is much less sensitive to ionization than the C–C* bond. For most of the amino acids, the C–C* bond is destabilized already at $\bar{z} = 0.2$ within 20–50 fs [Fig. 4(a)], whereas the C–N bond is mostly unaffected during the simulated 75 fs up to a $\bar{z} = 0.8$ [Fig. 4(c)]. The only exception is GLY, where the C–C* bond first breaks at approximately $\bar{z} = 0.3$ but shows an island of stability around $\bar{z} = 0.8$. Experimental studies of the fragmentation of alanine, due to ionization caused by ions, He^+, He^{2+}, and O^{5+}, have shown that the main fragmentation process is the dissociation of the C–C* bond, which agrees with what we observe in this study.[19] The C–R bond seems to be the most robust bond with respect to ionization in the systems investigated.

C. Carboxyl groups

The second observation that holds for all amino acids is that the hydrogen from the carboxyl group is ejected early in the simulations, even at low ionization states, $\bar{z} = 0.2$. This makes the remaining carboxyl group stable for higher ionization states. From the six amino acids, three (alanine, leucine, and methionine) ejected an intact COO– group that did not fragment during the 75 fs simulation at any of the ionization states tested here. The other three amino acids also keep their COO– group intact at higher ionization states than what causes the carbon-carbon backbone bond to break, but as illustrated in Fig. 4(d), the carbon-oxygen bonds in the carboxyl group is affected. The COO– group is stable until ionization levels of $\bar{z} = 0.9$ [Fig. 4(d)], and then the probability of dissociating to CO + O or complete fragmentation increases. In general, the COOH group is intact up to ionization levels of $\bar{z} = 0.4$ [Fig. 5(b)], after which it loses the hydrogen atom. Again, larger amino acids are more robust with respect to ionization. As can be seen in Fig. 6, the additional side-chain hydroxyl group in THR shows a similar stability behavior.

Looking at the case of glycine in detail, the bond integrity has a slight minimum at the ionization state just before the carboxyl hydrogen leaves, but once the hydrogen has left the group, the carbon-oxygen bond is more stable again (see supplementary material, Fig. SI.9). This is caused by the hydrogen leaving the group neutralizing the group somewhat. The effect of this is that the system, in this case the carboxyl group, is actually more stable at higher ionization states since that causes the hydrogen to leave and in reality makes the effective nuclear charge of the remaining group lower.

1. Amino group hydrogen dissociation

The amine group of hydrogen-bonds is mostly resilient to ionization of all hydrogen-bonds considered. The bonds are considered equivalent, but all amino acids, with the exception of THR, retain their amino-hydrogen atoms up to an ionization level that equals to the number of hydrogen atoms (Fig. 5).

D. Methyl groups

Methyl groups are analyzed in terms of their binding to the backbone and their dissociation, respectively, as shown in Fig. 7. The

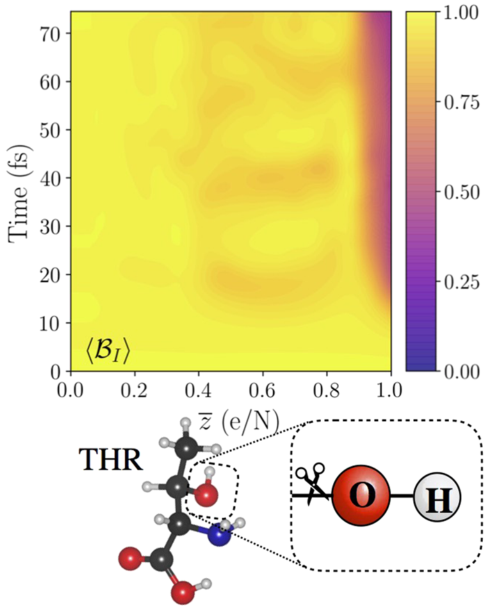

FIG. 6. The bond integrity of the side-chain-hydroxyl group resembles the bond integrity of the C*–O bond on the carboxyl group.

© Author(s) 2019

methyl C–R bond is significantly more stable than the C–H bond. Hydrogen atoms are generally dissociated around $\overline{z} = 0.35$. Similar to the carboxyl group, there is a region with a high probability of an intact methyl group, before the hydrogen atoms dissociate. Once hydrogen is removed, the C–R bond is stabilized until approximately ionization levels of $\overline{z} = 0.7 - 0.9$. Interestingly, the hydrogen atoms seem to leave all at once, with a very low probability of finding CH_2 or CH.

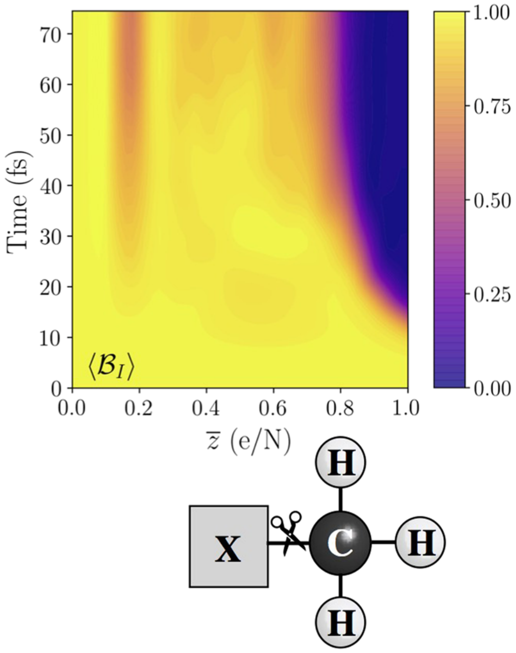

FIG. 7. Bond integrity of the methyl group to the side-chain. Already at an ionization stage of $\overline{z} = 0.3 - 0.4$, the hydrogen atoms have dissociated from the methyl group, leaving only the carbon atom bonded to the side-chain until $\overline{z} = 0.8$. See Fig. 5 for details on the hydrogen dissociation.

1. The role of sulfur

Methionine (MET) is the only sulfur-containing amino acid considered here. Upon ionization, we can see that the S-methyl complex detaches from the backbone at a lower degree of ionization than the methyl group that detaches from sulfur, as seen in Figs. 8(a) and 8(b). Similar to other bonds that do not involve hydrogen, we can see a stability island for certain degrees of ionization, as displayed in Fig. 8. The valley appears at $\overline{z} = 0.5 - 0.8$, beginning roughly at a charge of +11, equal to the number of hydrogen atoms on methionine.

E. Characteristic trends for specific bonds

We also analyze the trends in the breaking of specific bonds with respect to amino acid size or weight. We investigate the bond between the backbone C and the R group, the backbone C and the carboxyl O, and the backbone C–C* bond and the backbone C–N bond. In general, the trends with respect to weight/size are weak to nonexistent. However, in particular, for the C–R and C–C bonds, individual amino acids show a strengthening of the

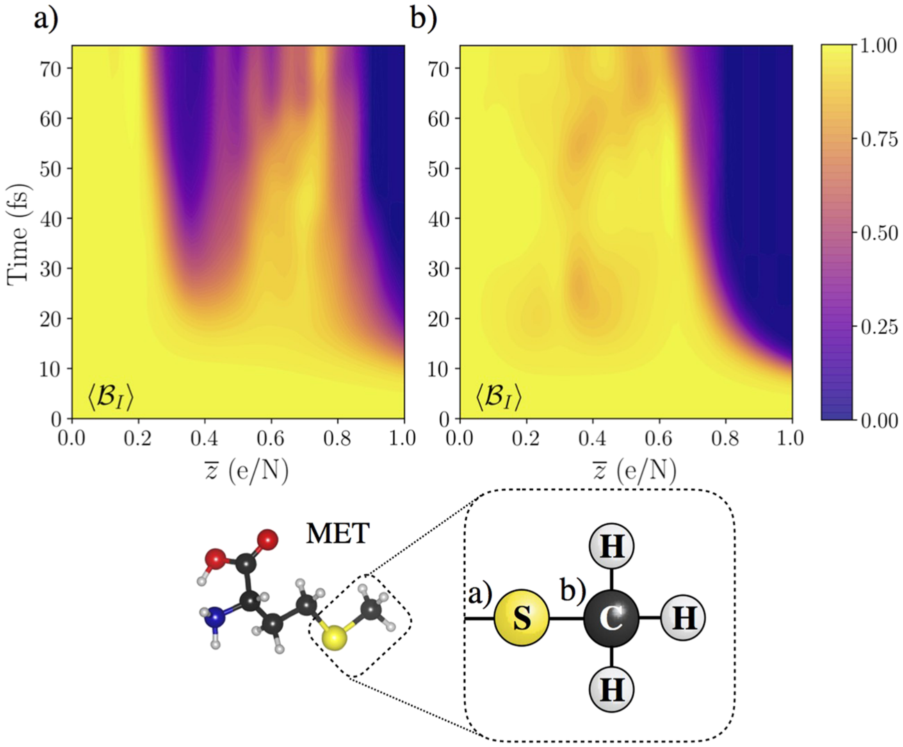

FIG. 8. Bond integrity of the bonds associated with sulfur, (a) S-side-chain and (b) S-Methyl. The S-side-chain bond in (a) shows a significant stability island, with a primary dissociation threshold of $\overline{z} = 0.3$, while being reattached and detached at $\overline{z} = 0.5$ and $\overline{z} = 0.8$, respectively. The restabilization of the bond coincides with the loss of hydrogen on the adjacent methyl group. In (b), we see that the S-methyl bond has a more monotonous behavior, with a distinct threshold of approximately $\overline{z} = 0.7$.

© Author(s) 2019

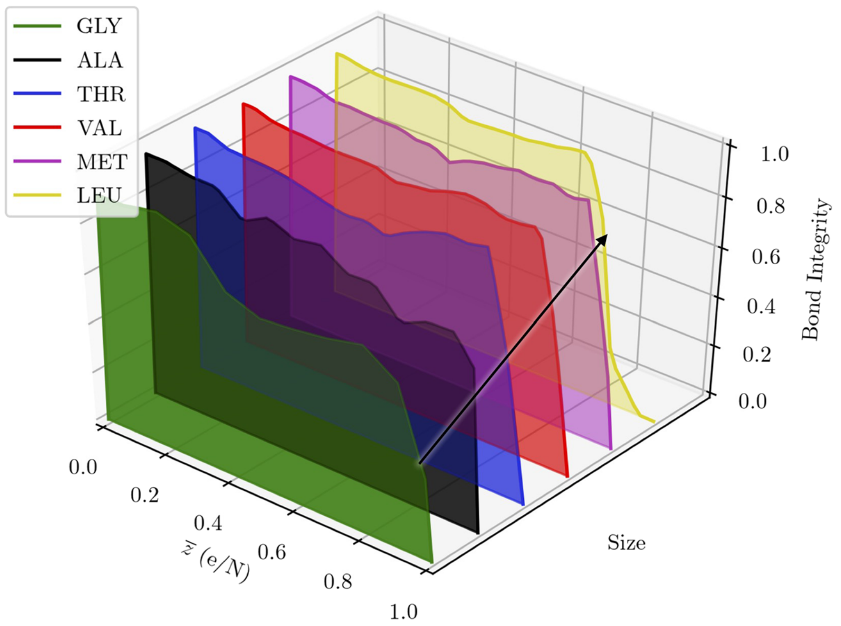

FIG. 9. Average bond integrity of the C–N bond between 25 and 75 fs. The trend indicates that in larger amino acids, the C–N breaks at a slightly lower level of ionization.

bond when the hydrogen atoms have dissociated. The C–N bond shows a weak trend with respect to size, where the larger amino acids show a slightly higher affinity to dissociate the amine-group, as displayed in Fig. 9.

IV. DISCUSSION

For computational reasons, our study is limited to six amino acids. We have picked amino acids with a spread in size, which we hypothesized to have an impact on the stability. From the six amino acids we have simulated here, leucine is very common in proteins, and methionine, on the other hand, is rare. We have focused our study on general trends reflecting how the average amino acid in a protein behaves, and the trends we describe are general, at least for the amino acids investigated here. Since proteins contain a large number of amino acids of different kinds, trends in the dynamics caused by the ionization that are not amino acid specific are most relevant in an imaging perspective. Some differences between how the different amino acids behave exist but are not discussed in detail here. It is fair to say that the amino acids studied here behave similarly, with an exception for the smallest one, glycine, which is discussed in Sec. III C. In the supplementary material, we display the bond integrity for individual amino acids separately in Figs. SI.1–SI.8.

A general consideration is that only bonds to hydrogen break quicker than 15 fs. Since the hydrogen atoms do not contribute significantly to photon scattering in comparison to the heavier atoms, a pulse length of 15 fs or less would result in robust imaging, regardless of pulse intensity. At moderate levels of ionization, as quantified by a charge-state lower than the number of hydrogen atoms per amino acid, only the C–C* bond in the backbone shows a significant sensitivity. This bond breaks already at an ionization level of $\bar{z} = 0.1$, after around 20 fs from the point of ionization. This corroborates the experimental results of Schlathölter *et al.*, who investigated the fragmentation of ubiquitin under intense 70 fs pulses of 90 eV photons. They discovered no nondissociative triple ionization, while claiming that the protein as a whole responds to ionization as a collection of small peptides.[52] In the light of our result, we interpret the most likely dissociation channel to be a breaking of the amino acid carbon-carbon bond. Another general observation is that, except for the backbone carbon-carbon bond, hydrogen bonds are severed first. The removal of the hydrogen atoms offers some stability increase to the amino acid, or fragments like COO−. In imaging of a large protein, the ability of the hydrogens to leave will be limited, which in turn might affect the stability of the amino acids. On the other hand, the fragmentation of the heavier atoms is also slowed down by neighboring atoms.

Our study of the fragmentation and the charge dynamics of ultracharged amino acids is relevant for imaging using XFEL as well as in electron diffraction experiments. Our simulations indicate that there is a difference, shared by all the molecules simulated here, in how stable the different bonds in the amino acids are. This knowledge is important for both understanding the damage process itself and interpreting diffraction patterns. Our results are not directly transferable to larger systems such as proteins, but they give an indication of how the fragmentation of proteins will happen.

SUPPLEMENTARY MATERIAL

See the supplementary material for additional information on individual amino acids and validation simulations.

ACKNOWLEDGMENTS

Computational resources were supplied through the Swedish National Infrastructure for Computing (SNIC) through Uppsala Multidisciplinary Center for Advanced Computational Science (UPPMAX) under Project No. SNIC 2019/8-30 and the National

© Author(s) 2019

Supercomputing Center (NSC) under Project No. SNIC 2018/3-221. The methods used in this project were developed with the support from the Swedish Research Council (VR) Grant No. 637-2013-7303 and the Swedish Foundation for Strategic Research (SSF) under Grant No. ICA16-0037. C.C. acknowledges the Swedish Foundation for Strategic Research, the Swedish Research Council (2013-3940), the Swedish Research Council via the Röntgen-Ångström Cluster, the Carl Trygger Foundation, the Helmholtz Association through the Center for Free-Electron Laser Science at DESY, and the Australian Research Council's Centre of Excellence Programme.

REFERENCES

[1] R. Neutze, R. Wouts, D. van der Spoel, E. Weckert, and J. Hajdu, "Potential for biomolecular imaging with femtosecond X-ray pulses," Nature **406**, 752–757 (2000).

[2] A. Aquila, A. Barty, C. Bostedt, S. Boutet, G. Carini, D. dePonte, P. Drell, S. Doniach, K. H. Downing, T. Earnest, H. Elmlund, V. Elser, M. Gühr, J. Hajdu, J. Hastings, S. P. Hau-Riege, Z. Huang, E. E. Lattman, F. R. N. C. Maia, S. Marchesini, A. Ourmazd, C. Pellegrini, R. Santra, I. Schlichting, C. Schroer, J. C. H. Spence, I. A. Vartanyants, S. Wakatsuki, W. I. Weis, and G. J. Williams, "The linac coherent light source single particle imaging road map," Struct. Dyn. **2**, 041701 (2015).

[3] A. Barty, C. Caleman, A. Aquila, N. Timneanu, L. Lomb, T. A. White, J. Andreasson, D. Arnlund, S. Bajt, T. R. M. Barends, M. Barthelmess, M. J. Bogan, C. Bostedt, J. D. Bozek, R. Coffee, N. Coppola, J. Davidsson, D. P. DePonte, R. B. Doak, T. Ekeberg, V. Elser, S. W. Epp, B. Erk, H. Fleckenstein, L. Foucar, P. Fromme, H. Graafsma, L. Gumprecht, J. Hajdu, C. Y. Hampton, R. Hartmann, A. Hartmann, G. Hauser, H. Hirsemann, P. Holl, M. S. Hunter, L. Johansson, S. Kassemeyer, N. Kimmel, R. A. Kirian, M. Liang, F. R. N. C. Maia, E. Malmerberg, S. Marchesini, A. V. Martin, K. Nass, R. Neutze, C. Reich, D. Rolles, B. Rudek, A. Rudenko, H. Scott, I. Schlichting, J. Schulz, M. M. Seibert, R. L. Shoeman, R. G. Sierra, H. Soltau, J. C. H. Spence, F. Stellato, S. Stern, L. Strüder, J. Ullrich, X. Wang, G. Weidenspointner, U. Weierstall, C. B. Wunderer, and H. N. Chapman, "Self-terminating diffraction gates femtosecond X-ray nanocrystallography measurements," Nat. Photonics **6**, 35–40 (2012).

[4] A. V. Martin, J. K. Corso, C. Caleman, N. Timneanu, and H. M. Quiney, "Single-molecule imaging with longer X-ray laser pulses," IUCrJ **2**, 661–674 (2015).

[5] R. Henderson, "The potential and limitations of neutrons, electrons and X-ray for atomic-resolution microscopy of unstained biological molecules," Q. Rev. Biophys. **28**, 171–193 (1995).

[6] J. C. H. Spence, "Outrunning damage: Electrons vs X-rays—timescales and mechanisms," Struct. Dyn. **4**, 044027 (2017).

[7] S. P. Weathersby, G. Brown, M. Centurion, T. F. Chase, R. Coffee, J. Corbett, J. P. Eichner, J. C. Frisch, A. R. Fry, M. Guehr, N. Hartmann, C. Hast, R. Hettel, R. K. Jobe, E. N. Jongewaard, J. R. Lewandowski, R. K. Li, A. M. Lindenberg, I. Makasyuk, J. E. May, D. McCormick, M. N. Nguyen, A. H. Reid, X. Shen, K. Sokolowski-Tinten, T. Vecchione, S. L. Vetter, J. Wu, J. Yang, H. A. Duerr, and X. J. Wang, "Mega-electron-volt ultrafast electron diffraction at slac national accelerator laboratory," Rev. Sci. Instrum. **86**, 073702 (2015).

[8] P. Zhu, Y. Zhu, Y. Hidaka, L. Wu, J. Cao, H. Berger, J. Geck, R. Kraus, S. Pjerov, Y. Shen, R. I. Tobey, J. P. Hill, and X. J. Wang, "Femtosecond time-resolved MeV electron diffraction," New J. Phys. **17**, 063004 (2015).

[9] Y. Murooka, N. Naruse, S. Sakakihara, M. Ishimaru, J. Yang, and K. Tanimura, "Femtosecond time-resolved MeV electron diffraction," Appl. Phys. Lett. **98**, 251903 (2011).

[10] R. F. Egerton, "Outrun radiation damage with electrons?," Adv. Struct. Chem. Imaging **1**, 5 (2015).

[11] J. de Vries, R. Hoekstra, R. Morgenstern, and T. Schlathölter, J. Phys. B **35**, 4373 (2002).

[12] J. de Vries, R. Hoekstra, R. Morgenstern, and T. Schlathölter, Eur. Phys. J. **24**, 161 (2003).

[13] J. de Vries, R. Hoekstra, R. Morgenstern, and T. Schlathölter, Phys. Rev. Lett. **91**, 053401 (2003).

[14] R. Bredy, J. Bernard, L. Chen, B. Wei, A. Salmoun, T. Bouchama, M. C. Buchet-Poulizac, and S. Martin, Nucl. Instrum. Methods Phys. Res. B **235**, 392 (2005).

[15] T. Schlathölter, F. Alvarado, S. Bari, A. Lecointre, R. Hoekstra, V. Bernigaud, B. Manil, J. Rangama, and B. Huber, ChemPhysChem **7**, 2339 (2006).

[16] F. Alvarado, S. Bari, R. Hoekstra, and T. Schlathölter, Phys. Chem. Chem. Phys. **8**, 1922 (2006).

[17] G. Weber and L. Young, J. Biol. Chem. **239**, 1424 (1964).

[18] N. Dookeran, T. Yalcin, and A. Harrison, "Fragmentation reactions of protonated alpha-amino acids," J. Mass Spectrom. **31**, 500–508 (1996).

[19] S. Bari, P. Sobocinski, J. Postma, F. Alvarado, R. Hoekstra, V. Bernigaud, B. Manil, J. Rangama, B. Huber, and T. Schlathölter, "Fragmentation of α- and β-alanine molecules by ions at Bragg-peak energies," J. Chem. Phys. **128**, 074306 (2008).

[20] J. M. Soler, E. Artacho, J. D. Gale, A. García, J. Junquera, P. Ordejón, and D. Sánchez-Portal, "The SIESTA method for *ab-initio* order-*N* materials simulation," J. Phys. Condens. Mater **14**, 2745–2779 (2002).

[21] G. Kolesov, O. Grånäs, R. Hoyt, D. Vinichenko, and E. Kaxiras, "Real-time TD-DFT with classical ion dynamics: Methodology and applications," J. Chem. Theory Comput. **12**, 466–476 (2016).

[22] J. T. Margraf, D. S. Ranasinghe, and R. J. Bartlett, "Automatic generation of reaction energy databases from highly accurate atomization energy benchmark sets," Phys. Chem. Chem. Phys. **19**, 9798–9805 (2017).

[23] H. J. C. Berendsen, D. van der Spoel, and R. van Drunen, "GROMACS: A message-passing parallel molecular dynamics implementation," Comput. Phys. Commun. **91**, 43–56 (1995).

[24] E. Lindahl, B. Hess, and D. van der Spoel, "GROMACS 3.0: A package for molecular simulation and trajectory analysis," J. Mol. Mod. **7**, 306–317 (2001).

[25] D. van der Spoel, E. Lindahl, B. Hess, G. Groenhof, A. E. Mark, and H. J. C. Berendsen, "GROMACS: Fast, flexible and free," J. Comput. Chem. **26**, 1701–1718 (2005).

[26] B. Hess, C. Kutzner, D. van der Spoel, and E. Lindahl, "GROMACS 4: Algorithms for highly efficient, load-balanced, and scalable molecular simulation," J. Chem. Theory Comput. **4**, 435–447 (2008).

[27] H. J. C. Berendsen and W. F. van Gunsteren, "Molecular dynamics simulations: Techniques and approaches," in *Molecular Liquids-Dynamics and Interactions*, NATO ASI C 135, edited by A. J. Barnes *et al.* (Reidel, Dordrecht, The Netherlands, 1984), pp. 475–500.

[28] T. Darden, D. York, and L. Pedersen, "Particle mesh Ewald: An N-log(N) method for Ewald sums in large systems," J. Chem. Phys. **98**, 10089–10092 (1993).

[29] U. Essmann, L. Perera, M. L. Berkowitz, T. Darden, H. Lee, and L. G. Pedersen, "A smooth particle mesh Ewald method," J. Chem. Phys. **103**, 8577–8592 (1995).

[30] C. Caleman, P. J. van Maaren, M. Hong, J. S. Hub, L. T. Costa, and D. van der Spoel, "Force field benchmark of organic liquids: Density, enthalpy of vaporization, heat capacities, surface tension, compressibility, expansion coefficient and dielectric constant," J. Chem. Theory Comput. **8**, 61–74 (2012).

[31] D. van der Spoel, P. J. van Maaren, and C. Caleman, "GROMACS molecule & liquid database," Bioinformatics **28**, 752–753 (2012).

[32] M. J. Frisch, G. W. Trucks, H. B. Schlegel, G. E. Scuseria, M. A. Robb, J. R. Cheeseman, J. A. Montgomery, Jr., T. Vreven, K. N. Kudin, J. C. Burant, J. M. Millam, S. S. Iyengar, J. Tomasi, V. Barone, B. Mennucci, M. Cossi, G. Scalmani, N. Rega, G. A. Petersson, H. Nakatsuji, M. Hada, M. Ehara, K. Toyota, R. Fukuda, J. Hasegawa, M. Ishida, T. Nakajima, Y. Honda, O. Kitao, H. Nakai, M. Klene, X. Li, J. E. Knox, H. P. Hratchian, J. B. Cross, C. Adamo, J. Jaramillo, R. Gomperts, R. E. Stratmann, O. Yazyev, A. J. Austin, R. Cammi, C. Pomelli, J. W. Ochterski, P. Y. Ayala, K. Morokuma, G. A. Voth, P. Salvador, J. J. Dannenberg, V. G. Zakrzewski, S. Dapprich, A. D. Daniels, M. C. Strain, O. Farkas, D. K. Malick, A. D. Rabuck, K. Raghavachari, J. B. Foresman, J. V. Ortiz, Q. Cui, A. G. Baboul, S. Clifford, J. Cioslowski, B. B. Stefanov, G. Liu, A. Liashenko, P. Piskorz, I. Komaromi, R. L. Martin, D. J. Fox, T. Keith, M. A. Al-Laham, C. Y. Peng, A. Nanayakkara, M. Challacombe, P. M. W. Gill, B. Johnson, W. Chen, M. W. Wong, C. Gonzalez, and J. A. Pople, GAUSSIAN 03, Revision C.02, Gaussian, Inc., Wallingford CT, 2004).

[33] R. Krishnan, J. Binkley, R. Seeger, and J. Pople, "Self-consistent molecular-orbital methods. 20. Basis set for correlated wave-functions," J. Chem. Phys. **72**, 650–654 (1980).

© Author(s) 2019

[34] A. McLean and G. Chandler, "Contracted Gaussian-basis sets for molecular calculations .1. Second row atoms, Z = 11–18," J. Chem. Phys. **72**, 5639–5648 (1980).

[35] M. Glukhovtsev, A. Pross, M. McGrath, and L. Radom, "Extension of Gaussian-2 (G2) theory to bromine-containing and iodine-containing molecules - use of effective core potentials," J. Chem. Phys. **103**, 1878–1885 (1995).

[36] L. Curtiss, M. McGrath, J. Blaudeau, N. Davis, R. Binning, and L. Radom, "Extension of Gaussian-2 theory to molecules containing third-row atoms Ga–Kr," J. Chem. Phys. **103**, 6104–6113 (1995).

[37] J. Blaudeau, M. McGrath, L. Curtiss, and L. Radom, "Extension of Gaussian-2 (G2) theory to molecules containing third-row atoms K and Ca," J. Chem. Phys. **107**, 5016–5021 (1997).

[38] J. Wang, R. M. Wolf, J. W. Caldwell, P. A. Kollman, and D. A. Case, "Development and testing of a general amber force field," J. Comput. Chem. **25**, 1157–1174 (2004).

[39] W. L. Jorgensen, J. Chandrasekhar, J. D. Madura, R. W. Impey, and M. L. Klein, "Comparison of simple potential functions for simulating liquid water," J. Chem. Phys. **79**, 926–935 (1983).

[40] J. S. Hub, C. Caleman, and D. van der Spoel, "Organic molecules on the surface of water droplets - an energetic perspective," Phys. Chem. Chem. Phys. **14**, 9537–9545 (2012).

[41] P. Souvatzis, "Uquantchem: A versatile and easy to use quantum chemistry computational software," Comput. Phys. Commun. **185**, 415–421 (2014).

[42] C. Caleman, G. Huldt, F. R. N. C. Maia, C. Ortiz, F. G. Parak, J. Hajdu, D. van der Spoel, H. N. Chapman, and N. Timneanu, "On the feasibility of nanocrystal imaging using intense and ultrashort X-ray pulses," ACS Nano **5**, 139–146 (2011).

[43] C. Caleman, C. Ortiz, E. Marklund, F. Bultmark, M. Gabrysch, F. G. Parak, J. Hajdu, M. Klintenberg, and N. Tîmneanu, "Radiation damage in biological material: Electronic properties and electron impact ionization in urea," Europhys. Lett. **85**, 18005 (2009).

[44] L. Kleinman and D. M. Bylander, "Efficacious form for model pseudopotentials," Phys. Rev. Lett. **48**, 1425–1428 (1982).

[45] J. P. Perdew, M. Ernzerhof, and K. Burke, "Rationale for mixing exact exchange with density functional approximations," J. Chem. Phys. **105**, 9982–9985 (1996).

[46] H. O. Jönsson, C. Östlin, H. A. Scott, H. N. Chapman, S. J. Aplin, N. Tîmneanu, and C. Caleman, "Freedam—A webtool for free-electron laser-induced damage in femtosecond x-ray crystallography," High Energy Density Phys. **26**, 93–98 (2018).

[47] P. Souvatzis and A. M. N. Niklasson, "First principles molecular dynamics without self-consistent field optimization," J. Chem. Phys. **140**, 044117 (2014).

[48] C. W. Bauschlicher, "A comparison of the accuracy of different functionals," Chem. Phys. Lett. **246**, 40–44 (1995).

[49] F. L. Hirshfeld, "Bonded-atom fragments for describing molecular charge densities," Theor. Chim. Acta **44**, 129–138 (1977).

[50] C. Fonseca Guerra, J.-W. Handgraaf, E. J. Baerends, and F. M. Bickelhaupt, "Voronoi deformation density (vdd) charges: Assessment of the mulliken, bader, hirshfeld, weinhold, and vdd methods for charge analysis," J. Comput. Chem. **25**, 189–210 (2004).

[51] E. R. Davidson and S. Chakravorty, "A test of the hirshfeld definition of atomic charges and moments," Theor. Chim. Acta **83**, 319–330 (1992).

[52] T. Schlathölter, G. Reitsma, D. Egorov, O. Gonzalez-Magaña, S. Bari, L. Boschman, E. Bodewits, K. Schnorr, G. Schmid, C. D. Schröter, R. Moshammer, and R. Hoekstra, "Multiple ionization of free ubiquitin molecular ions in extreme ultraviolet free-electron laser pulses," Angew. Chem., Int. Ed. **55**, 10741–10745 (2016).

© Author(s) 2019